J. Fluid Mech. (2024), *vol*. 982, A6, doi:10.1017/jfm.2024.104

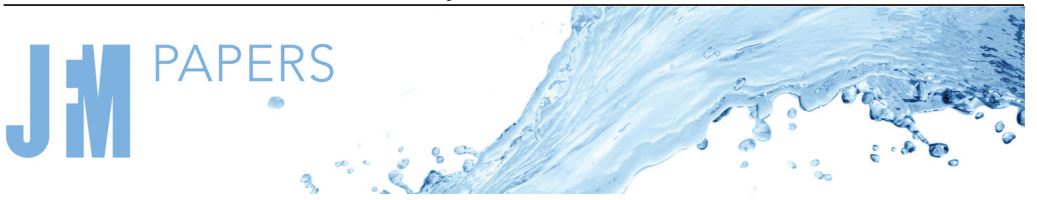

The dynamics of impinging plumes from a moving source

E.L. Newland[1],† **and A.W. Woods**[1]

[1]Institute for Energy and Environmental Flows, Department of Earth Science, University of Cambridge, Madingley Road, Cambridge CB3 0EZ, UK

(Received 12 July 2023; revised 29 November 2023; accepted 23 January 2024)

We present the results from a series of experiments investigating the dynamics of gravity currents which form when a dense saline or particle-laden plume issuing from a moving source interacts with a horizontal surface. We define the dimensionless parameter P as the ratio of the source speed, u_a, to the buoyancy speed, $(B_0/z_0)^{1/3}$, where B_0 and z_0 are the source buoyancy flux and height above the horizontal surface, respectively. Using our experimental data, we determine that the limiting case in which $P = P_c$ the gravity current only spreads downstream of the initial impact point occurs when $P_c = 0.83 \pm 0.02$. For $P < P_c$, from our experiments we observe that the plume forms a gravity current that spreads out in all directions from the point of impact and the propagation of the gravity current is analogous to a classical constant-flux gravity current. For $P > P_c$, we observe that the descending plume is bent over and develops a pair of counter-rotating line vortices along the axis of the plume. The ensuing gravity current spreads out downstream of the source, normal to the motion of the source. Analogous processes occur with particle-laden plumes, but there is a second dimensionless parameter S, the ratio of the particle fall speed, v_s, to the vertical speed of a plume in a crossflow, $(B_0/u_a z_0)^{1/2}$. For $S \ll 1$, particles remain well mixed in the plume and a particle-driven gravity current develops. For $S \gg 1$, particles separate from the plume prior to impacting the boundary which leads to a fall deposit and no gravity current. We discuss these results in the context of deep-sea mining.

Key words: plumes/thermals, gravity currents, sediment transport

1. Introduction

Mining in the deep sea is a rapidly emerging industry for obtaining resources for the energy transition, such as poly-metallic nodules, cobalt-rich crust and massive sulphide

† Email address for correspondence: e.newland@ucl.ac.uk

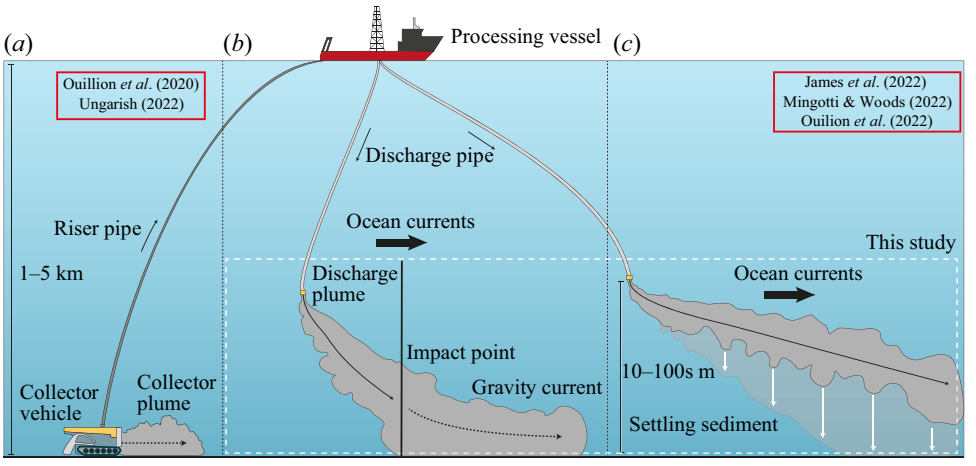

Figure 1. Schematic diagram highlighting the dynamics of deep-sea mining plumes. (*a*) Collector plumes formed by the discharge of sediment-laden mixture at the sea floor. (*b*) Sediment-laden plumes issued tens to hundreds of metres above the sea floor that impact the sea floor to form turbulent gravity currents. (*c*) Sediment laden plumes issued tens to hundreds of metres above the sea floor in which the particle load separates from the plume prior to impacting the seafloor. The solid black arrows represent the motion of particle-laden plumes, the dashed black arrows represent the motion of particle-driven gravity currents and the solid white arrows represent the motion of sedimenting particles.

deposits (Sharma 2017; Hein, Koschinsky & Kuhn 2020; Jones, Elliott & Nguyen-Tien 2020). In the case of poly-metallic nodules, robotic collectors mechanically remove the partially or completely buried ore from the seabed. The nodules are then transported to a surface vessel, along with a dense mixture of seawater and sediment, via a riser pipe for separation and further processing. As a result of this operation, a dense sediment-rich fluid is produced which must be discharged back into the ocean. The disposal of this sediment-laden fluid has the potential to contaminate the water column and sea floor with toxic species and the fluid mechanical processes of sediment dispersion and dissolution need to be understood in order to assess these environmental impacts (Jones *et al.* 2021).

Some of the sediment-laden fluid collected from the seafloor is released directly from the rear of the moving collector vehicle located on the seafloor to form a dense flow that spreads out across the seabed, often termed a collector plume (figure 1*a*). The dynamics of these flows have been investigated by Ouillon *et al.* (2021) using direct numerical simulation of a moving spherical source of buoyancy located directly above a solid surface. The authors found that when the speed of source, u_a, is much lower than the characteristic speed of the gravity current, u_g, the flow spreads out in all directions and tends to the form of an axisymmetric constant-flux gravity current (Chen & List 1976; Britter 1979). However, as the source speed exceeds the gravity current speed the flow evolves downstream of the source, spreading laterally in a fashion similar to a two-dimensional (2-D) finite release gravity current (Hoult 1972). Ungarish (2022) presented a detailed comparison of the numerical results of Ouillon *et al.* (2021) with a box model formulation based on the classical theory of turbulent gravity currents.

In addition to particles suspended by the collector vehicle, other sediment-rich fluid may be discharged from the processing vessel into the water column to form dense sediment plumes (figure 1*b*). The dynamics of these flows have been the subject of some attention (Muñoz-Royo *et al.* 2021; James, Mingotti & Woods 2022; Mingotti & Woods 2022; Ouillon *et al.* 2022), with the majority of the work focused on the case in which there

is either a background ambient current or the plume issues from a moving source. James *et al.* (2022) build on the classical theory of single-phase turbulent plumes in a uniform crossflow (Scorer 1958; Slawson & Csanady 1967; Hoult, Fay & Forney 1969; Hewett, Fay & Hoult 1971) to explore the effect of particle-separation on the dynamics. This study is complimented by the work of Mingotti & Woods (2022) that explores the impact of the initial buoyancy flux of the plume on the dispersal of the sediment load through the water column. From their experiments, the authors found that in order to reduce the dispersal distance of the sediment, the particulate waste collected at the seafloor can be mixed with seawater obtained near the bottom of the ocean and discharged close to the seabed. This should ensure that the interstitial fluid in the plume is neutrally or negatively buoyant, and the sediment-laden flow sinks to the sea floor as a dense plume consisting of a pair of counter-rotating vortices (Scorer 1958; Turner 1960; Csanady 1965; Hoult & Weil 1972; Abdelwahed 1978; Zhang & Ghoniem 1993; Ernst *et al.* 1994), which enhances the entrainment of fluid into the flow.

If these descending plumes reach the seafloor, there is likely to be a transition to a gravity-current-type flow that spreads out across the seabed. How the gravity current evolves will determine the dispersal distance of the sediment. Kaye & Hunt (2007) investigated the impingement of single-phase plumes in a quiescent environment on a solid horizontal surface and found that, after a short transition zone, the gravity-driven flow tends to form a constant flux axisymmetric gravity current. Hogg, Hallworth & Huppert (2005) considered the specific case of a 2-D gravity current, supplied by single-phase and particle-laden plumes, in a weak uniform ambient crossflow, in which the initial gravity current speed exceeds that of the current. The authors show that after impacting the floor, a fraction of the flow propagates upstream and reaches a steady-state distance from the point of impact, due to the opposing ambient current, and a fraction of the flow propagates downstream at a rate equal to the sum of the crossflow and gravity current speeds.

In this paper, we build on these earlier works, especially those of Ouillon *et al.* (2021), Ungarish (2022) and James *et al.* (2022), through an experimental study in which we systematically examine the dynamics of gravity currents that form when a dense single-phase or particle-laden plume, with buoyancy flux B_0, issuing from a moving source at height z_0 above the sea bed, descends through the water column and then spreads out over the base of the experimental tank. First, we investigate the morphology of the gravity currents as a function of the source speed with a series of experiments on single-phase plumes. The dynamics of the gravity currents are controlled by the balance between the speed of the source issuing the plume, u_a, and the characteristic speed associated with the buoyancy of the plume as it impacts the seafloor, u_g, where

$$u_g \sim \left(\frac{|B_0|}{z_0}\right)^{1/3}, \tag{1.1}$$

as given by the dimensionless parameter

$$P = \frac{u_a}{u_g} = \frac{u_a}{(|B_0|/z_0)^{1/3}}. \tag{1.2}$$

It is important to note the relationship between the dimensionless parameter P and the length scale $L_b = B_0/u_a^3$, introduced by Devenish *et al.* (2010), that represents the distance over which the effect of a moving ambient dominates the dynamics of the flow. The dimensionless variable P also represents the ratio of the height of source z_0 to the length scale L_b, such that $P = (z_0/L_b)^{1/3}$.

When $P \ll 1$, the relative speed of the source is low, and the gravity-driven flow spreads out in all directions from the point of impact. For $P \gg 1$, the gravity current

evolves exclusively downstream of the point of impact. In § 3, using measurements of our experiments, we determine the critical value of P above which the flow spreads exclusively downstream from the point of impact. We also show that the circulation that develops in the plume has an important effect on the structure and propagation of the ensuing gravity currents.

We then assess the impact of particle separation on the gravity currents formed by the interaction of a particle-laden plume with a solid interface, focusing on the case $P > 1$. The impact of the separation of particles can be expressed by the ratio, S, of the fall speed of the particles, v_s, to the initial speed of the gravity current (James *et al.* 2022),

$$u_p \sim \left(\frac{|B_0|}{u_a z_0}\right)^{1/2}, \tag{1.3}$$

so that

$$S = \frac{v_s}{u_p} = \frac{v_s}{u_a} P^{3/2}. \tag{1.4}$$

When $S \ll 1$, the fall speed of the particles is small in comparison with the gravity current speed and we expect the particles to be carried far downstream from the point of impingement by the gravity current. For $S \gg 1$, the particle load sediments from the descending plume, and settles on the seabed prior to forming a gravity current (James *et al.* 2022; Mingotti & Woods 2022). In the discussion, we consider the implication of this study for sediment plumes formed during deep-sea mining.

It is important to note that throughout this study we consider the case in which the dynamics of the descending plume are not affected by the ambient stratification of the ocean. We can evaluate the impact of an ambient stratification by comparing the height of the plume source, z_0, to the characteristic length scale over which the background stratification impacts the dynamics of a plume in a moving ambient (Mingotti & Woods 2022),

$$z_s \sim \left(\frac{B_0}{u_a N^2}\right)^{1/3}, \tag{1.5}$$

where N is the Brunt–Väisälä buoyancy frequency of the ambient fluid, which in the deep ocean takes a value in the range $N \sim 10^{-4}$–10^{-5}. In the case in which the plume source height is much greater than the stratification length scale ($z_0 \gg z_s$), we expect that the background stratification impacts the dynamics of the flow such that the descending plume forms an intermediate intrusion in the water column prior to impacting the seafloor, as discussed in Mingotti & Woods (2022). However, when the source height is small in comparison with the stratification length scale ($z_0 \ll z_s$), we expect the descending plume to impact the seafloor and spread out as a gravity-driven flow, the dynamics of which form the basis of this study.

2. Methods

A series of laboratory experiments were performed in which a saline solution or mixture of fresh water and dense particles was issued from a moving source at a height, z_0, above the base of a Perspex tank. The Perspex tank had a cross-sectional area of 1.30×1.30 m and was filled to a constant depth of 0.32 m with fresh water of density $\rho_a = 1000\,\mathrm{kg\,m^{-3}}$. The base and one side of the tank was back-lit using multiple electroluminescent light sheets (LightTape by Electro-LuminiX Lighting Corp.) and each experiment was filmed

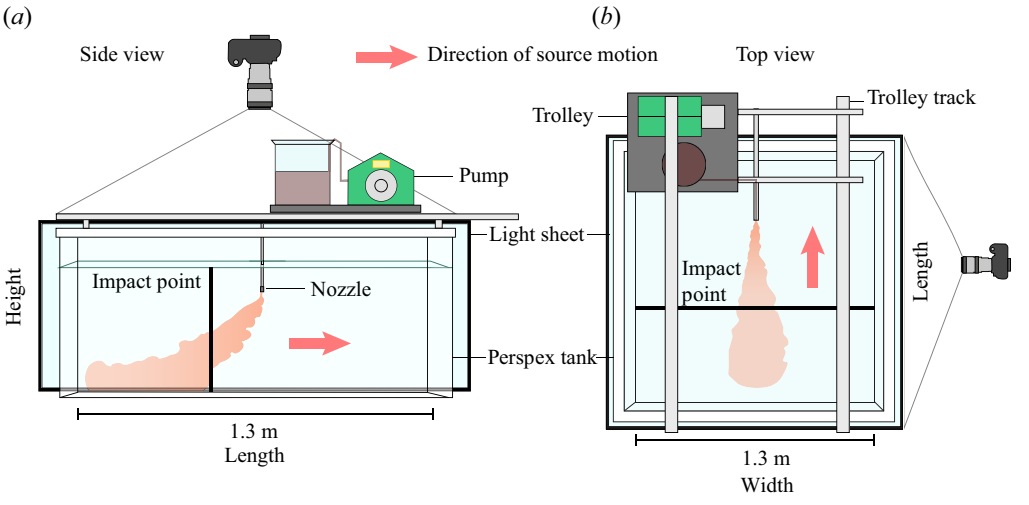

Figure 2. Experimental set-up: (*a*) side view of the experimental tank; (*b*) top view of the experimental tank.

using two Nikon D5300 digital cameras at a frame rate of 50 Hz positioned as shown in figure 2.

The source nozzle was attached to a motorised trolley via an extendable arm and the height of the source, z_0, was varied between each experiment in the range 0.05–0.3 m. The motorised trolley traversed the top of the tank on a set of metal tracks at a constant speed, u_a, and an experiment consisted of a single pass of the experimental tank by the source nozzle. The saline solution or fluid–particle mixture was supplied to the tank through a nozzle with an internal diameter of $d_0 = 5$ mm via a Watson Marlow peristaltic pump at a constant volumetric flow rate, Q_0. To ensure that the flow was turbulent on impact, we kept the Reynolds number of the flow at the source, $Re = d_0 u_0/\nu$, where u_0 is the outlet velocity at the source and ν is the kinematic viscosity of the water greater than 1800. The source buoyancy flux of the fluid or particle-fluid mixture is given by the relationship

$$B_0 = \frac{\rho_m - \rho_a}{\rho_a} g Q_0, \tag{2.1}$$

where ρ_m is the density of the saline solution or bulk density of the fluid–particle mixture, ρ_a the density of the ambient fluid, and g is the acceleration of gravity. For the experiments in which we investigate the dynamics of particle-laden flows, we used a mixture of fresh water, of density $\rho_f = 998\,\mathrm{kg\,m^{-3}}$, and silicon carbide particles (Washington Mills), of density $\rho_p = 3206\,\mathrm{kg\,m^{-3}}$. The mixture had a bulk density given by the relationship $\rho_m = c_0\rho_p + (1 - c_0)\rho_f$, where c_0 is the particle volume concentration. We continuously stirred the fluid–particle mixture prior to and throughout an experiment with a mechanical stirrer to ensure the particles remained well mixed in the fluid. Over a systematic series of experiments, the median length of the major axis of the particles, D_p, was varied over the range 22.8–212 µm. The particle mixtures consist of a distribution of particle lengths, determined in accordance with the FEPA (The Federation of the European Producers of Abrasives) regulations. For particles smaller than $D_p \leq 53$ µm (FEPA-F Microgrits), the variation in the particle length is expressed using the 25th (D_{25}) and 75th (D_{75}) percentiles, whereas for particles greater than $D_p > 53$ µm (FEPA-F Macrogrits), the variation in the particle length is expressed using the 3rd (D_3) and 94th (D_{94}) percentiles. Therefore, as a simple and consistent estimate of the variation in the size of the particles about the median

value, we define

$$\left.\begin{aligned} \sigma_D &= \frac{D_{75} - D_{25}}{2}, \quad \text{for } D_p \leq 53\,\mu\text{m}, \\ \sigma_D &= \frac{D_{94} - D_3}{4}, \quad \text{for } D_p > 53\,\mu\text{m}. \end{aligned}\right\} \tag{2.2}$$

We find that the maximum value is $\sigma_D \sim 15\,\%$, however for the majority of particles sizes $\sigma_D < 10\,\%$. We list the median particle length, D_p, alongside the estimates of σ_D in table 1 for the range of particles sizes used in this study. To estimate the vertical fall speed of the particles, v_s, we use Stokes law such that

$$v_s = \frac{1}{18}\frac{\rho_p - \rho_a}{\mu_a} g D_p^2. \tag{2.3}$$

This approximation is based on the assumption that the particles are spherical in shape, however previous studies of particle-laden flows that use the same silicon carbide particles, which are stated to be blocky/hexagonal in shape, have shown that the measured sedimentation speed shows good agreement with the estimates based on Stokes law (Mingotti & Woods 2015; Newland & Woods 2021). We list the estimates of v_s as a function of particle size, D_p, in table 1 alongside the error in the fall speed associated with the variation in particle size, σ_D, which are consistent with measurements of the fall speeds of the same particles presented in Mingotti & Woods (2015).

The videos taken of each experiment were subsequently processed and analysed in MATLAB. To enhance the clarity of the fluid and particle motion, we removed the background from the experimental videos by subtracting a frame taken prior to the start of each experiment. The experimental frames were then converted first into grey-scale images by selecting a single colour channel from the digital images and then into binary images, in which the dyed fluid was represented by a 1 and the background was represented by a 0. The binary images were created by applying the in-built MATLAB threshold algorithm, *imbinarize*, which uses the Otsu method (Otsu 1979) to select a threshold intensity value that maximises the inter-class intensity variance between the pixels that represent the dyed fluid and the pixels that represent the background, to each row of the grey-scale images. The outer edge of the dyed fluid was then identified in each frame to extract bulk measurements of the flow such as the length and width of the gravity current formed on the base of the tank. To ensure that we do not include any data that may be affected by the presence of the tank walls, we exclude all experimental frames in which the outer edge of the gravity currents are within 5 cm of the tank walls, a distance comparable with the depth of the gravity currents.

3. Single-phase experiments

We now describe the single-phase gravity currents for different values of the parameter P which captures the ratio of the source speed to the buoyancy speed of the flow. We estimate the critical value of P, which we denote as P_c, at which there is a transition from currents which spread in all directions from the point of impingement ($P < P_c$) to those which only spread downstream ($P > P_c$). We then present quantitative measurements of the lateral propagation and morphology of the gravity currents for both regimes, including a discussion of the impact of the circulation that develops for experiments in which $P > P_c$.

Experiment	Q_0 ($\times 10^{-6}$)	B_0 ($\times 10^{-6}$)	ρ_f	c_0	$D_p \pm \sigma_D$ ($\times 10^{-6}$)	v_s ($\times 10^{-3}$)	z_0	t_0	u_a	P	S
a	5.9	−3.8	1065	—	—	—	0.10	0.48	0.00	0.000	—
b	5.9	−3.8	1065	—	—	—	0.20	2.51	0.00	0.000	—
c	5.9	−3.8	1065	—	—	—	0.30	4.13	0.00	0.000	—
d	5.9	−3.8	1065	—	—	—	0.10	0.10	0.011	0.33	—
e	5.9	−3.8	1065	—	—	—	0.10	0.61	0.012	0.35	—
f	5.9	−3.8	1065	—	—	—	0.10	0.24	0.014	0.42	—
g	5.9	−3.8	1065	—	—	—	0.10	0.55	0.025	0.75	—
h	5.9	−3.8	1065	—	—	—	0.10	0.72	0.027	0.86	—
i	5.9	−3.8	1065	—	—	—	0.10	0.48	0.041	1.21	—
j	5.9	−3.8	1065	—	—	—	0.10	1.35	0.065	1.94	—
k	5.9	−3.8	1065	—	—	—	0.20	1.32	0.010	0.38	—
l	5.9	−3.8	1065	—	—	—	0.20	1.32	0.011	0.39	—
m	5.9	−3.8	1065	—	—	—	0.20	1.68	0.024	0.88	—
n	5.9	−3.8	1065	—	—	—	0.20	1.71	0.038	1.42	—
o	5.9	−3.8	1065	—	—	—	0.20	4.20	0.062	2.31	—
p	5.9	−3.8	1065	—	—	—	0.30	1.98	0.008	0.35	—
q	5.9	−3.8	1065	—	—	—	0.30	3.96	0.026	1.09	—
r	5.9	−3.8	1065	—	—	—	0.30	7.42	0.042	1.80	—
s	5.9	−3.8	1065	—	—	—	0.30	10.93	0.062	2.66	—
1	5.9	−3.6	1000	0.028	12.8 ± 0.9	0.22 ± 0.03	0.05	0.50	0.119	2.85	0.009
2	5.9	−3.6	1000	0.028	22.8 ± 1.5	0.70 ± 0.09	0.05	0.55	0.116	2.78	0.028
3	5.9	−3.6	1000	0.028	44.5 ± 2.0	2.68 ± 0.24	0.05	0.45	0.121	2.91	0.110
4	5.9	−3.6	1000	0.028	63.0 ± 9.3	5.37 ± 1.57	0.05	0.58	0.085	2.03	0.184
5	5.9	−3.6	1000	0.028	63.0 ± 9.3	5.37 ± 1.57	0.05	0.31	0.121	2.91	0.220
6	5.9	−3.6	1000	0.028	106.0 ± 8.8	15.2 ± 2.53	0.05	0.20	0.110	2.66	0.596
7	5.9	−3.6	1000	0.028	12.8 ± 0.9	0.22 ± 0.03	0.10	2.50	0.122	3.69	0.013
8	5.9	−3.6	1000	0.028	22.8 ± 1.5	0.70 ± 0.09	0.10	1.11	0.114	3.44	0.040
9	5.9	−3.6	1000	0.028	106.0 ± 8.8	15.2 ± 2.53	0.10	1.48	0.110	3.30	0.837
10	5.9	−3.6	1000	0.028	212.0 ± 17.5	60.8 ± 10.1	0.10	0.71	0.089	2.69	3.020
11	5.9	−3.6	1000	0.028	12.8 ± 0.9	0.22 ± 0.03	0.20	2.50	0.113	4.30	0.018
12	5.9	−3.6	1000	0.028	22.8 ± 1.5	0.70 ± 0.09	0.20	3.43	0.110	4.21	0.055
13	5.9	−3.6	1000	0.028	44.5 ± 2.0	2.68 ± 0.24	0.20	2.01	0.109	4.16	0.209
14	5.9	−3.6	1000	0.028	63.0 ± 9.3	5.37 ± 1.57	0.20	3.89	0.110	4.19	0.419
15	5.9	−3.6	1000	0.028	106.0 ± 8.8	15.6 ± 2.53	0.20	1.56	0.110	4.21	1.190
16	5.9	−3.6	1000	0.028	212.0 ± 17.5	60.8 ± 10.1	0.20	2.37	0.110	4.18	4.750

Table 1. Experimental parameters for (a–s) single-phase and (1–16) particle-laden impinging plumes from a moving source. Here Q_0 ($m^3\,s^{-1}$) is the source volume flux, B_0 ($m^4\,s^{-3}$) is the source buoyancy flux, ρ_f is the density of the plume fluid ($kg\,m^{-3}$), c_0 is the particle volume fraction, D_p is the average particle size (m), v_s is the Stoke fall speed of a particle ($m\,s^{-1}$), z_0 is the height of the source (m), t_0 is the virtual origin estimate (s), u_a ($m\,s^{-1}$) is the speed of the source, P is the dimensionless source speed and S is the dimensionless separation parameter.

3.1. *Critical P (P_c)*

Figure 3(*a*) presents frames of the side and top view of our experimental tank showing the instantaneous morphology of two experiments. Figure 3(*a*) displays an experiment in which the dimensionless source speed is less than the critical value, $P < P_c$, and the initial plume descends near-vertical and impacts the tank floor to form a gravity current that spreads out in all directions. In the stationary reference frame of the tank, the speed

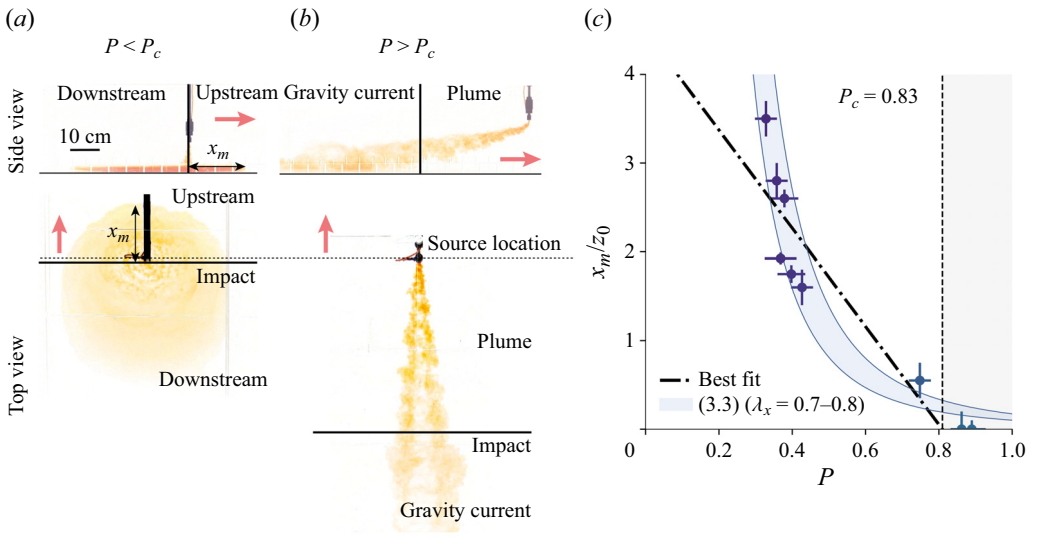

Figure 3. Experimental images from side and top of the tank for an experiment in which (*a*) $P < P_c$ and the gravity current spreads out in all directions from the point of impact (experiment *d*, $P = 0.33$) and (*b*) $P > P_c$ and the gravity current propagates only downstream from the point of impact (experiment *o*, $P = 2.31$). The red arrows represent the direction of source motion, the black arrows represent the maximum upstream distance, x_m. The dotted black line represents the source location. The black solid lines represent the location of plume impact. (*c*) The maximum distance of the upstream edge of the gravity current from the point of plume impact, x_m, scaled with source height, z_0, as a function of the dimensionless source speed, P. The black dot-dashed line represents the line of best fit, which is extrapolated to intersect the horizontal axis to determine the critical value, P_c, at which the upstream distance, x_m, vanishes to zero. The blue shaded area represents the estimate of the upstream distance, x_m (3.3), for the range of $\lambda_x = 0.7$–0.8 estimated from our experiments.

of the flow that spreads upstream from the point of impact decreases and the flow reaches a maximum steady-state distance from the impact point, x_m, at which the speed of the gravity current is equal to the speed of source, u_a. Figure 3(*b*) displays an experiment in which the dimensionless source speed is greater than the critical value, in which the initial plume is bent over by the relative motion of the ambient environment and the flow impacts the base of the tank to form a gravity current that evolves downstream from the point of impact. There is a transition from one regime to the other when $P = P_c$, and the gravity current does not spread upstream of the point of contact of the plume, $x_m \to 0$.

From our experimental images of the top view of the tank, we have measured the steady-state distance the gravity current travels upstream from the point of impact, x_m, as a function of the dimensionless source speed P and we show the results in figure 3(*c*). We can obtain an estimate of P_c, by plotting the line of best fit through the positive values of our experimental data of x_m, and extrapolating the line to intercept the x axis, at which point we define the critical value P_c. Using this method, we obtain a critical value $P_c = 0.83 \pm 0.02$, consistent with our qualitative observations that at $P = 0.75$ we observe a gravity current which spreads upstream from the point of impact and at $P = 0.86$ we observe a gravity current that evolves exclusively downstream from the point of impact.

3.2. $P < P_c$

Figure 4 displays a series of images, taken in the stationary reference frame of the tank, showing an experiment in which the dimensionless speed of the source, $P = 0.35$. Figure 4(*a*) is the side view of the tank and figure 4(*b*) is the top view of the tank. The horizontal black dot-dashed line represents the location at which the plume fluid first

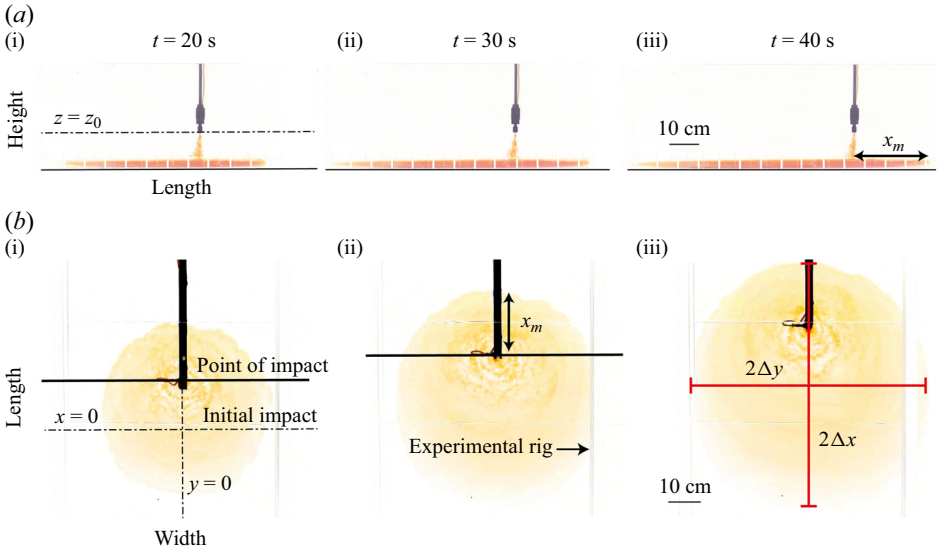

Figure 4. Series of experimental frames from experiment d ($P = 0.33$) showing (a) the side view and (b) the top view of the experimental tank at times, $t = 20$, 30 and 40 s after initial impact. The black dot-dashed lines represent the $y = 0$, $x = 0$ and $z = z_0$ axis. The black arrow represents the maximum distance the gravity current propagates upstream, x_m, from the point of impact. The black solid line represents the location of plume impact. The red solid lines represent the maximum width, $2\Delta y$ and maximum length, $2\Delta x$ of the flow. The white bars that obscure some of the flow are part of the experimental rig.

impacts the base of the tank and transitions to a gravity-driven flow. We define this point as $(x, y) = 0$, with the positive x-direction representing the direction of the motion of the source nozzle, which we term the upstream direction, and the negative x-direction representing the opposite direction to the motion of the source nozzle, which we term the downstream direction. The black solid lines represent the location at which the plume subsequently impacts the base of the tank. The source is moving at a constant speed, u_a. In this experiment, the speed of the source is small in comparison with the characteristic speed of the plume and the flow propagates radially after impact. The flow initially spreads out as a series of concentric high-concentration rings, which then merge after a critical distance is reached. Some of the fluid travels upstream from the point of impact and reaches a steady-state maximum distance, x_m (Figure 4b,ii). The flow also spreads laterally and forms a near-circular current. The red lines $2\Delta x$ and $2\Delta y$ represent the instantaneous maximum length and width of the current respectively.

In a quiescent environment, the radial propagation of an axisymmetric constant flux gravity current in the inertia-buoyancy regime depends on the source buoyancy flux, B_0, and time from the first impact of the plume, t, such that the position of the outer-edge of the current follows the relation (Chen & List 1976; Britter 1979)

$$r = \lambda B_0^{1/4} t^{3/4}. \tag{3.1}$$

Here, λ is a constant of proportionality, which has been determined experimentally to take a value between 0.75 and 0.85 (Chen & List 1976; Britter 1979; Kaye & Hunt 2007). To test this scaling for the propagation of the gravity currents, we first consider the initial conditions of the flow. On impact with the floor of the tank, the descending plume and, hence, gravity current has a finite non-zero volume, which scales with the radius of the plume on impact and therefore we assume that the gravity current issues from a virtual

origin at time $t = -t_0$. We obtain an estimate of the average virtual origin by plotting the width and length the gravity current, $\Delta y^{4/3}$ and $\Delta x^{4/3}$, as a function of time and extrapolate the lines of best fit to intersect with the x-axis. In figure 4(a), we plot the length scale associated with the virtual time origin, $x_0 = \bar{\lambda} B_0^{1/4} t_0^{3/4}$, using a mean value $\bar{\lambda}$ for each experiment, against the height of the source, z_0, and find that the virtual length origin is proportional to the height of the source such that, $x_0 \sim 0.2 z_0$. This result is consistent with the virtual origin scaling with the radius of the plume on impact, $x_0 \sim r_p = \alpha z_0$, where $\alpha = 0.16$ is the entrainment coefficient for a vertical plume, which suggests that after impact with the base of the tank, the gravity current quickly adjusts to the form of a self-similar constant flux gravity current.

In figure 5(b), we present the length Δx, dashed blue line, and width Δy, dot-dashed blue line, normalised by the scaling for the propagation of an axisymmetric constant-flux gravity current (3.1) as a function of time for two experiments. We find that both the maximum width and length of the gravity current scale with the relation (3.1), and in the examples presented in figure 5(b), the value of the constant of proportionality for the length, λ_x, is marginally greater than that for the width, λ_y. We can estimate the aspect ratio, $\Lambda = \lambda_x/\lambda_y$, and find that the gravity current spreads to form slightly elliptical flow, elongated in the streamwise direction. In figure 5(c), we present the values of λ_x, λ_y, and the aspect ratio, Λ, with the dimensionless source speed, P. For our experiments in which the source is stationary ($P = 0$), $\lambda_x = \lambda_y = 0.75 \pm 0.03$, consistent with previous experimental studies of axisymmetric gravity currents. However as P increases beyond value 0.4, there is an increase in λ_x and, in turn, an increase in the aspect ratio of the flow to a value $\Lambda = 1.15 \pm 0.02$ at $P = 0.75$, demonstrating that as P increases the gravity currents become elongated in the streamwise direction.

In addition to these measurements of the width and length of the gravity currents, we have measured the time-averaged shape of the flows. In figure 5(d), we show two examples of the time-averaged outer edge of the gravity currents normalised by the maximum width of the flow Δy at each time step, for experiments in which $P = 0$ and $P = 0.75$. The dashed black line in each plot represents a circle with an aspect ratio equal to 1. When $P = 0$, the time-averaged shape is well described as a circle. However, as P increases to value 0.75, the flow becomes elongated in the direction of the flow and is no longer axisymmetric (figure 5d).

It is of interest to consider the evolution of the front leading edge, the position of maximum width and the back trailing edge of the gravity current with time. In figures 6(a,i) and 6(a,ii), we plot the position of the front, maximum width and back of the gravity current, with time from the first impact of the plume, t, for experiments in which the dimensionless source parameter, (i) $P = 0.75$ and (ii) $P = 0.35$. In the stationary reference frame of the tank, the source is moving at a constant speed, u_a, in the x-direction, such that the position of the source and the position of the impact point of the plume are given by $u_a t$, represented by the dotted black lines in figures 6(a,i) and 6(a,ii). The flow that propagates upstream is arrested by the relative flow of the ambient environment, and reaches a maximum distance, x_m. We can obtain a simple estimate of the distance the flow travels upstream by equating the speed of the source, u_a to the speed of this upstream flow,

$$u_a = \tfrac{3}{4} \lambda_x B_0^{1/4} t^{-1/4}. \tag{3.2}$$

By substituting (3.2) into (3.1), we find the relation for the upstream distance (cf. Ungarish 2022)

$$x_m = \lambda_x^4 \left(\frac{3}{4u_a} \right)^3 B_0, \tag{3.3}$$

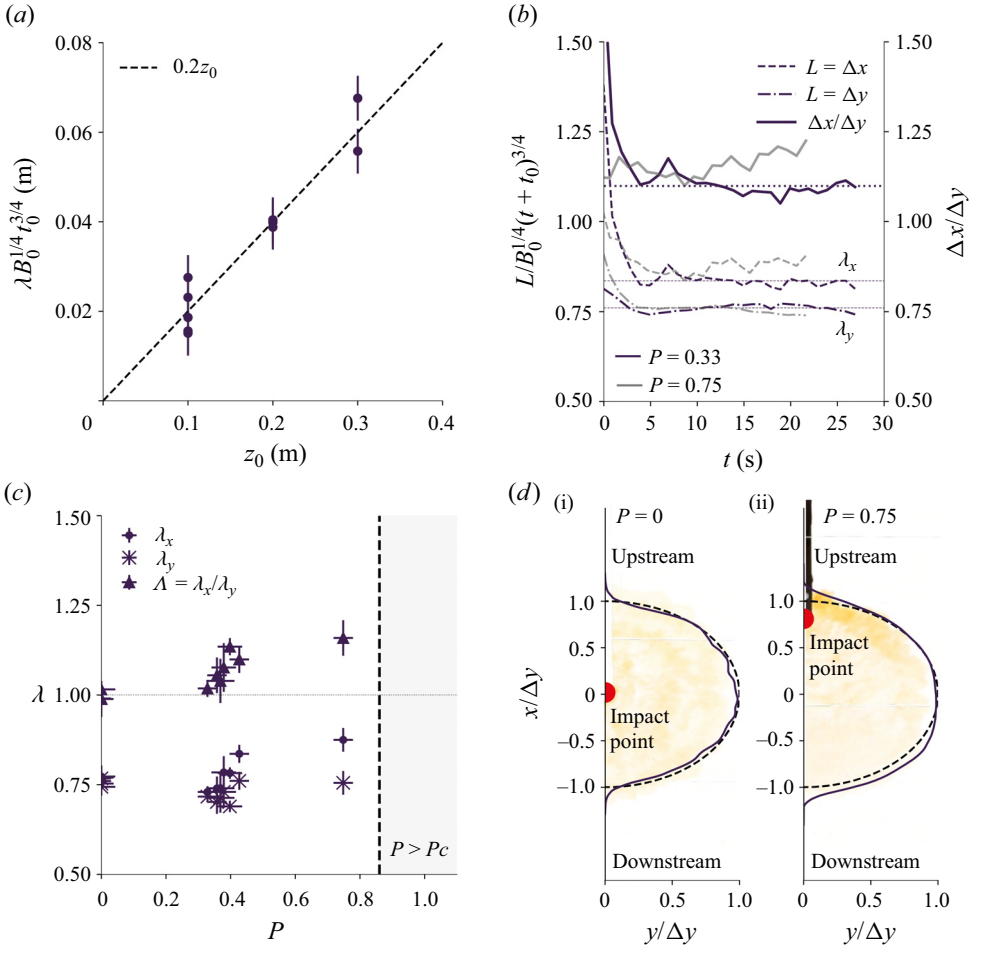

Figure 5. (*b*) The maximum length, Δx (dashed line), and width, Δy (dot-dashed line), normalised by the scaling for the propagation of an axisymmetric constant flux gravity current (3.1) on the left axis, and the ratio, $\Delta x/\Delta y$ (bold solid line) on the right axis as a function of time for experiment *d* ($P = 0.33$) in purple and experiment *g* ($P = 0.75$) in grey. The dotted black lines represents the steady-state values used to determine the coefficients λ_x, λ_y and Λ. (*c*) The coefficients λ_x (blue dots) and λ_y (blue crosses) and the steady-state aspect ratio (blue triangles) with the dimensionless source speed, P. The black dashed line represents the critical value of P above which the gravity current no longer propagates upstream from the point of impact. (*d*) Two examples of the time-averaged outer edge of the gravity currents that have been normalised by the maximum width of the flow, Δy at each time step for an experiment in which the source is (i) stationary, $P = 0$ (experiment *b*), and (ii) moving, $P = 0.75$ (experiment *g*).

and the time at which this condition is first satisfied

$$t_m = \frac{3x_m}{4u_a}. \tag{3.4}$$

In figure 3(*c*), we plot the length, x_m, (3.3) using the range of $\lambda_x = 0.7$–0.8 estimated from our experiments as a function of P and find good agreement with out experimental data. After time t_m we expect that the position of the front of the gravity current from the initial point of impact will be given by

$$x_f = x_m + u_a t. \tag{3.5}$$

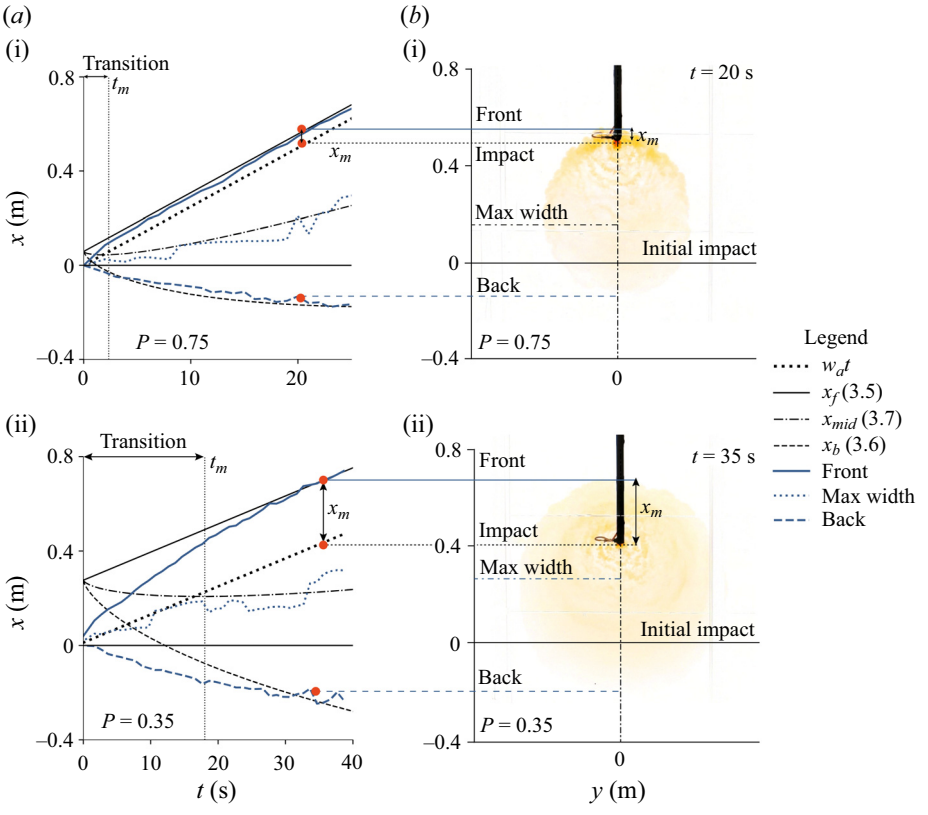

Figure 6. (*a*) The measured position of the front, back and max width point of the gravity currents from (i) experiment *g* and (ii) experiment *e*. The experimental measurements are represented by the dark blue lines and the theoretical predictions of (3.3)–(3.7) are represented by the black lines, as shown in the legend. The dashed black vertical line represents the transition time, t_m (3.4). (*b*) Experimental snapshots of the top view of the tank demonstrating the position of the front, back and max width of the gravity current for (i) experiment *g* at time $t = 20$ s after initial impact and (ii) experiment *e* at time $t = 35$ s after initial impact.

Our analysis of the shape of the gravity currents shows that the maximum length of the gravity current increases with time according to the relation (3.1). We can estimate the position of the trailing edge of the gravity current as the position of the front edge minus the increase in the length of the gravity current, such that

$$x_b = x_m + u_a t - 2\lambda_x B_0^{1/4}(t + t_0)^{3/4} \tag{3.6}$$

and, hence, the midpoint of the gravity current will follow the relation

$$x_{mid} = x_m + u_a t - \lambda_x B_0^{1/4}(t + t_0)^{3/4}. \tag{3.7}$$

In figures 6(*a*,i) and 6(*b*,i) we plot the estimates of (3.5)–(3.7) with time, using the values of λ_x and t_0 estimated above for each experiment. This figure reveals that for $t > t_m$, the experimental data tends to the scaling laws (e.g. (3.3)–(3.7)) for the leading and trailing edge of the gravity current. We also plot the position of the maximum width of the gravity current with time, which we find is located at the estimate of the midpoint of the gravity current in the along flow direction, according to (3.7). This analysis illustrates that for $P < P_c$, these gravity currents spread out in an analogous fashion to an axisymmetric gravity

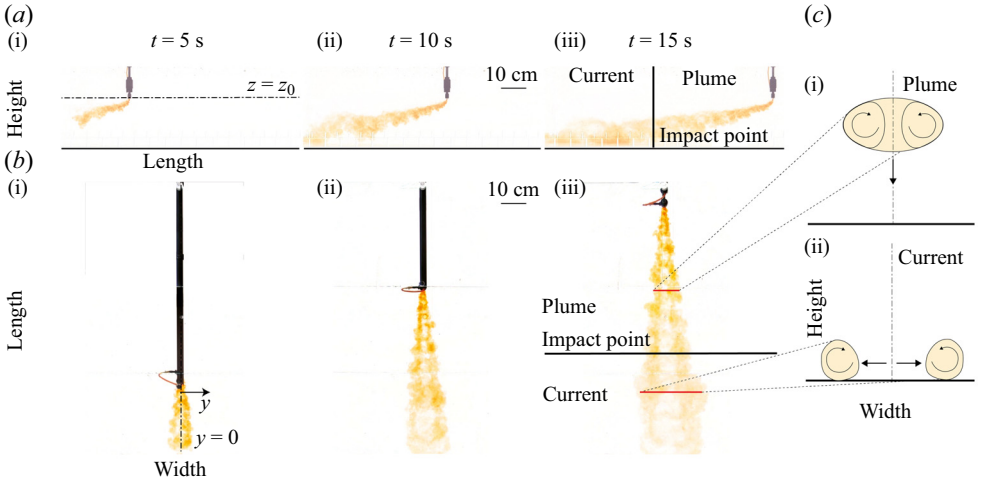

Figure 7. Series of experimental frames from experiment *o* ($P = 2.31$) showing (*a*) the side view and (*b*) the top view of the tank at times, $t = 5$, 10 and 15 s after the initial injection. The black dot-dashed line represents the $z = z_0$ axis, the black sold line represents the location of plume impact. (*c*) Schematic diagram illustrating a cross-section of (i) the descent of the plume and (ii) the propagation of the gravity current. The black arrows indicate the orientation of the circulation in the plume.

current centred about the midpoint of the flow, and that as the dimensionless source speed of the gravity current increases, the flow becomes elongated in the streamwise direction. As the dimensionless source speed increases, we observe a transition in the dynamics of the gravity current such that they evolve exclusively downstream from the point of impact, and are analogous to a 2-D finite release gravity current issuing from a line source. Therefore, we do not compare the scaling for an axisymmetric constant flux (3.1) with our experiments in which $P > P_c$.

3.3. $P > P_c$

Figure 7 presents a series of experimental frames taken from (*a*) the side of the tank and (*b*) the top of the tank for an experiment in which the speed of the source is fast in comparison to the buoyancy speed of the descending flow, $P = 2.31$. Figure 7(*a*) shows that after injection the initial plume is quickly bent over by the relative motion of the ambient fluid. The frames taken from the top of the tank (figure 7*b*) reveal that as the plume descends, the flow becomes localised into two distinct regions of high concentration, separated by a region of low concentration centred along the line followed by the moving source. As the flow evolves downstream the width of the high concentration regions increase and the distance between these regions also increases. Previous experimental and theoretical studies of buoyant plumes in a crossflow (Scorer 1958; Turner 1960; Csanady 1965; Hoult & Weil 1972; Abdelwahed 1978; Ernst *et al.* 1994) have described that a circulation develops in the plume in the form of a counter-rotating vortex pair along the axis of the flow, with the circulation orientated as shown in figure 7(*c*,i). Figure 7(*b*,iii) shows a frame in which the plume impacts the base of the tank, represented by the solid black line, and the flow transitions to a gravity-driven flow that spreads out laterally on the base of the tank. The striking feature of this flow is that the dense fluid remains localised in the vortex structures which then spread laterally from the centreline, separated by a distinct region of low concentration (figure 7*c*,ii).

To examine the time evolution of these flows, we show a time series of a line of pixels, oriented normal to the direction of the flow, from every frame of the top view of the tank (figure 8*a*,i). This image shows that soon after the injection of the fluid, the flow is concentrated into the two distinct vortex structures, separated by an area of low fluid concentration along the centreline of the flow. As the plume impacts the base of the tank (black solid line), the majority of the fluid remains partitioned in these structures with a distinct leading and trailing edge that both propagate laterally with time, with little to no fluid in the region that separates them. In figure 8(*a*,ii), we present a second time series of the same experiment in which we have normalised the width of the image to represent the instantaneous width of the flow, y_c, at each time step. This figure reveals that after the flow impacts the base of the tank to form the gravity-driven flow, the width of the high concentration structures, y_v tends to a constant fraction of the width of the total flow y_c. In figure 7(*b*) we present a series of horizontal light attenuation profiles taken from the time series in which the width of the image is normalised with the instantaneous width of the flow for experiments in which (i) $P = 1.44$ and (ii) $P = 2.31$. Each profile is coloured according to the time after impact, as shown in the legend. These profiles emphasise the presence of the low-concentration region along the axis of the flow, and highlight that the majority of the fluid is concentrated in the two line structures at the edge of flow, which tend to a constant width, y_v/y_c. On comparison of the two sets of profiles, the data show that as the dimensionless speed of the source, P, increases the characteristic width of the high-concentration structures, $\overline{y_v/y_c}$, increases. Furthermore, these profiles reveal that as time increases, the average light attenuation value in the head of the current decreases. This observation is consistent with the entrainment of ambient fluid into the head of the gravity current as the flow evolves, as described by Sher & Woods (2017) for 2-D finite release gravity currents.

We have created synthetic time series, such as that presented in figure 8(*a*,ii), for each of our experiments in which $P > 1$ and have measured the ratio of the width of the vortex to the width of the flow, y_v/y_c, as a function of time. We present the results in figure 8(*c*,i), with each line coloured according to the value of the dimensionless source speed, P, and time scaled with the descent time of the plume, t_c. Consistent with the example shown in figure 7(*a*,ii), we find that after the plume impacts the base of the tank, the ratio y_v/y_c tends to a near-constant value for all our experiments. As the dimensionless source speed, P, increases the vortex structures make up a larger fraction of the total width of the flow, (y_v/y_c increases). We present the average value of the ratio $\overline{y_v/y_c}$ for $t/t_c > 0$ in figure 7(*c*,ii) as a function of the dimensionless parameter P. This data shows that for the range of P in which our experiments lie, the fractional width of the vortex structures increases linearly with P and we obtain the empirical relation

$$\overline{y_v/y_c} = 0.16P + 0.32. \tag{3.8}$$

However, we expect that as the dimensionless source speed P increases beyond the values attained in this study, there will be a transition in behaviour as the width of the vortex structures are limited by the width of the flow.

We now compare the rate of lateral propagation of these vortex structures with that of a 2-D finite release gravity current. The descending plume impacts the base of the tank and transitions into a gravity-driven flow with buoyancy equal to the buoyancy per unit length of the plume, $B_0/2u_a$. The motion of a 2-D gravity current depends on a balance of buoyancy and inertia so that the distance of the outer edge of the flow from the centreline

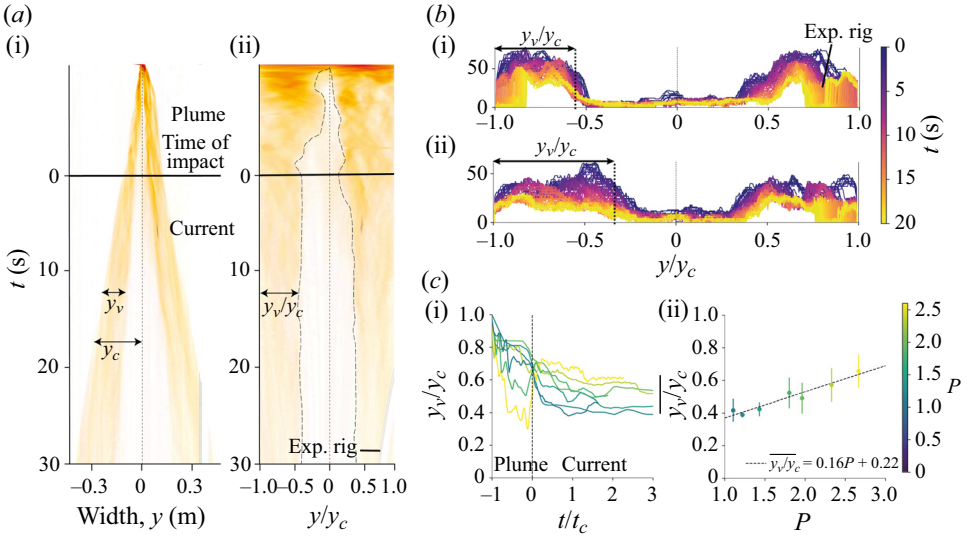

Figure 8. (*a*,i) Horizontal time series taken perpendicular to the direction of the source motion from the top view of the tank, for experiment *o* ($P = 2.31$). The length y_c represents the instantaneous width of the flow and the length y_v represents the instantaneous width of the vortex structures. (*a*,ii) Horizontal time series in which the width of the image has been normalised to the width of the flow, y_c, at each time step. The black dashed lines represent the inner edge of the vortex structures. The black solid line represents the time at which the flow first impacts the base of the tank. The white stripe in bottom right corner of the image is an area of the frame obstructed by the experimental rig. (*b*) Horizontal light attenuation profiles taken across the time series in which the width is normalised to the width of the flow (*a*,ii), for (i) experiment *n* ($P = 1.44$) and (ii) experiment *o* ($P = 2.31$). Each profile is coloured according to the time after impact. (*c*,i) The ratio of the vortex width to the flow width y_v/y_c as a function of time, normalised with the descent time of the plume. Each line is coloured according to the value of the dimensionless source speed P. (*c*,ii) The steady-state vortex width, $\overline{y_v/y_c}$ as a function of P. The black dashed line represents the line of best fit through the data.

scales as (Hoult 1972)

$$y = \zeta \left(\frac{B_0}{2u_a} \right)^{1/3} t^{2/3}, \tag{3.9}$$

where ζ is a constant of proportionality, that for lock-exchange experiments has a value 1.5–1.6 (Huppert & Simpson 1980; Marino, Thomas & Linden 2005; Sher & Woods 2015). On impact with the base of the tank, the plume has a finite volume and momentum flux, and the gravity-driven flow is established with an initial non-zero volume. To account for the initial volume of the gravity current, we assume that the flow evolves from a virtual origin at time $t = -t_0$. We obtain an estimate for the value of the time t_0, by plotting the distance of the outer edge of the gravity current, $y^{3/2}$, as a function of time. We extrapolate the line of best fit to intersect the x axis, as shown in figure 9(*a*).

The example profiles displayed in figure 9(*a*) show that as the dimensionless source speed, P, increases, the virtual origin time, t_0, increases. This relationship can be rationalised by considering the initial volume of the gravity current, V_0. The initial volume of the gravity current is determined by the volume of the plume on impact, V_p. Therefore, if we assume that a bent-over plume has a cylindrical cross-sectional area and that the gravity current is supplied by half of the volume of the plume on impact, we find that

$$V_0 \sim \frac{V_p}{2} = \frac{\pi}{2} r_p^2, \tag{3.10}$$

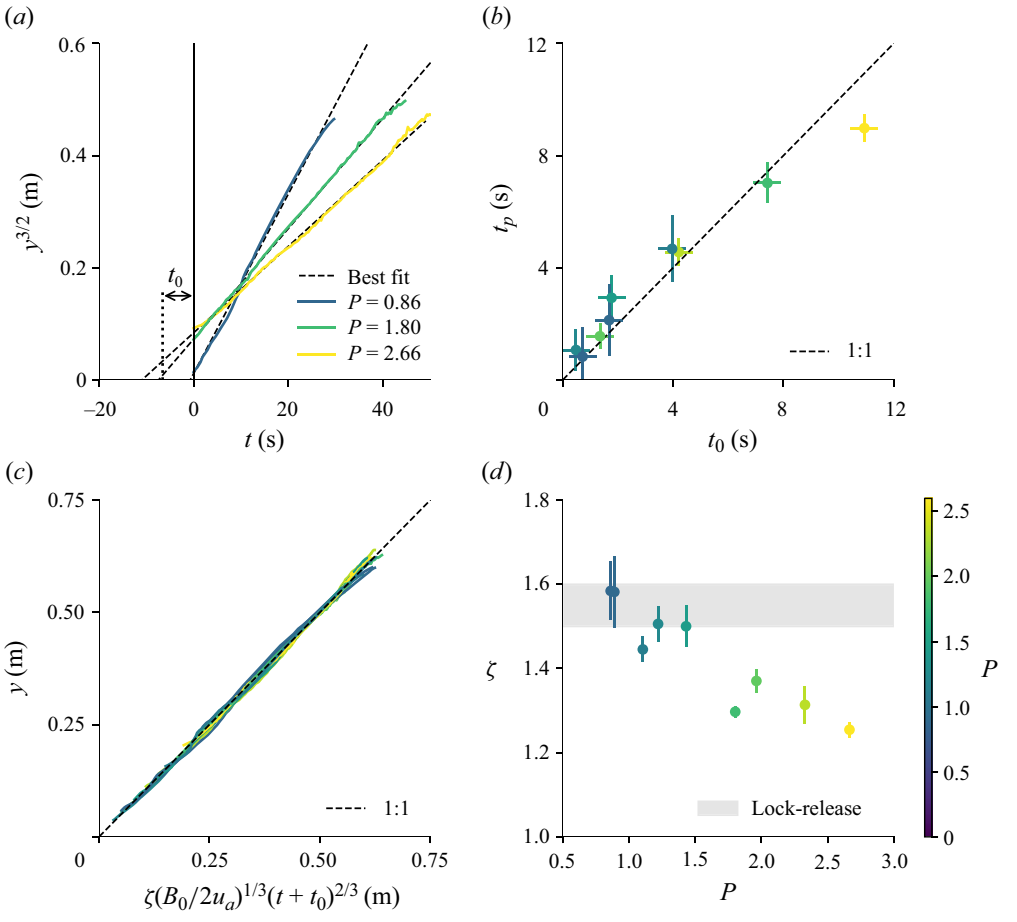

Figure 9. (*a*) Example profiles of the distance of the outer edge of the flow from the centreline, $y^{3/2}$, used to determine the time t_0 to the virtual origin. The black dashed lines represent the lines of best fit to the profiles. (*b*) The estimate of the virtual origin based on the initial volume flux of the gravity current, t_p (3.12), with the estimate of the virtual origin from the profiles in (*a*). (*c*) The distance of the outer edge of the gravity-driven flow from the centreline, y, with the estimate of the propagation of a 2-D finite-volume gravity current (3.9). (*d*) The coefficient ζ, determined by calculating the gradient of the lines in (*a*) with the dimensionless parameter P. The grey-shaded area represents the range of values of ζ determined from lock-exchange experiments. Each line is coloured with respect to the value of the dimensionless source speed P of that experiment.

where $r_p = \beta z_0$ is the radius of the plume on impact, $\beta = 0.4$ is the entrainment coefficient of a bent over plume and z_0 is the source height (Turner 1966; Hewett *et al.* 1971; James *et al.* 2022). This equation demonstrates that an increase in source height, z_0, and hence an increase in P (1.2), results in an increase in the initial volume of the gravity current for a fixed buoyancy and, therefore, the flow appears to be released from a more distant virtual origin.

We can estimate the time associated with the virtual origin in terms of the initial volume of the gravity current, by appealing to the work of Sher & Woods (2015). In this study the authors present the following empirical relation for the volume of a 2-D gravity current:

$$\frac{V}{y_0} = (0.31 \pm 0.02)y, \tag{3.11}$$

where y_0 is the initial gravity current length and y is the position of the nose of a gravity current with time, as given by (3.9). We can estimate the time, t_p, at which the volume of a 2-D gravity current (3.11) equals the initial volume of a gravity current, V_0 (3.10), formed due to the impingement of a bent-over plume by substituting (3.9) and (3.10) into (3.11), such that

$$t_p = \left(\frac{\pi r_p}{0.62\zeta}\right)^{3/2} \left(\frac{2u_a}{B_0}\right)^{1/2}, \tag{3.12}$$

where ζ is estimated from the gradient of the lines shown in figure 9(a) and y_0 is given by the radius of the plume on impact, r_p. In figure 3.9(b) we show the time t_p, as a function of the virtual origin time, t_0, measured from the profiles displayed in figure 9(a). This graph demonstrates that the position and time of the virtual origin is consistent with the initial volume of the gravity current per unit length matching the volume of the plume per unit length on impact with the base of the tank.

In figure 9(c), we compare the position of the outer-edge of the gravity current as a function of time with the relation (3.9), in which we determine the value of ζ from the gradients of the profiles displayed in figure 9(a). As shown in the legend, the colour of each line depends on the value of P. We find that for each experiment the position of the outer-edge of the flow scales with (3.9). In figure 9(d), we present the value of ζ as a function of P. This data reveals that for experiments in which $P < 1.5$, the coefficient ζ is consistent with the estimates obtained for lock-exchange gravity currents. However, as the speed of the source increases, we observe a significant decrease in the value of ζ, which represents a decrease in the lateral speed of the flow.

Here, it is of interest to compare the structure of the present gravity-driven flow with that of other finite-volume gravity currents. In the present case, we observe a gravity current in which the fluid is concentrated in a large vortex structure at the head of the flow, with a distinct leading and trailing edge, that is separated from the source region by an area of very low concentration. This is in contrast to the structure of classical finite-volume 2-D gravity current in which the flow consists of a head, in which some of the fluid is concentrated, with a trailing region of fluid that extends all the way back to the position of release (Sher & Woods 2015). However, the structure of the present flow displays some similarities with that of finite-volume axisymmetric gravity current, in which a ring vortex develops at the head of the current and the tail of the flow separates from the position of release (Patterson *et al.* 2006; Samasiri & Woods 2015), suggesting that the initial vorticity in the plume influences the subsequent development of the gravity current.

4. Particle-laden plumes

In the following section, we explore the dynamics of gravity currents that form by the interaction of particle-laden plumes with a solid boundary. We focus on the case in which the speed of the source is greater than the characteristic buoyancy speed of the flow ($P > P_c$) and investigate the effect of varying the dimensionless separation parameter S on the dispersal of particles in the flow. In our experimental frames, the particles are black and represented by the dark regions and the interstitial fluid is dyed red.

4.1. *Qualitative observations*

Figure 10 presents images from two experiments in which we vary the dimensionless separation parameter, S (§ 1, (1.4)), to highlight the two end-member regimes that we observe in our experiments in which (a) $S \ll 1$ and particles remain coupled to the plume

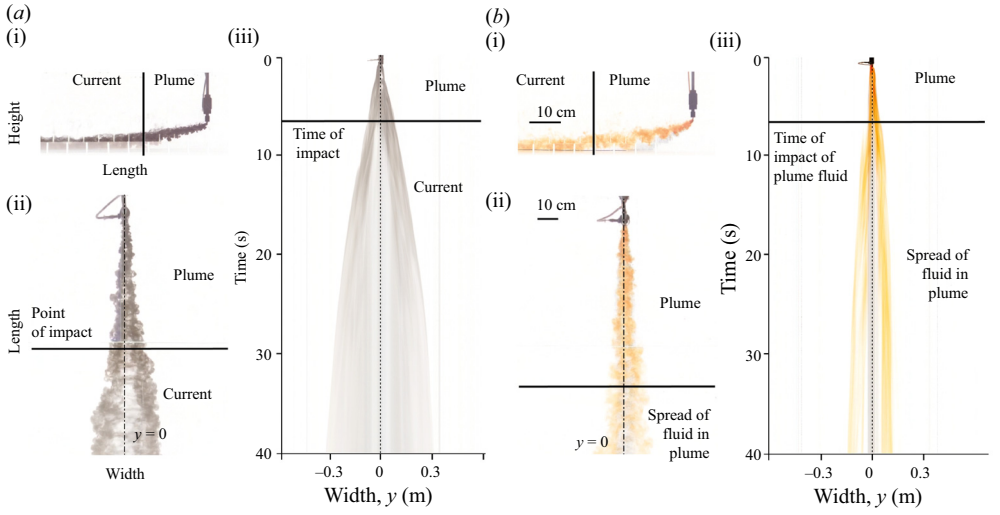

Figure 10. Experimental images from (*a*) experiment 7 in which $S = 0.013$ and particles remain coupled to the plume and impact the base of the tank to form a particle-driven gravity current and (*b*) experiment 10 in which $S = 3.02$ and particles separate from plume prior to impacting the base of the tank to form a fall deposit. (i) Experimental frames from the side view and (ii) from the top view of the tank. Each frame is taken 15 s after the initial injection of fluid. (iii) Horizontal time series taken perpendicular to the direction of the source motion from the top view of the tank. The black solid lines in each panel represent the location or time at which the plume impacts the base of the tank.

as the flow descends and impacts the base of the tank to form a particle-driven gravity current and (*b*) for which $S > 1$ and particles separate from the plume prior to impacting the base of the tank to form a fall deposit instead of a particle-driven gravity current. In each of the cases (*a*,*b*), part (i) shows an instantaneous frame of the experiment from the side of the tank, part (ii) shows an instantaneous frame of the experiment from the top of the tank and part (iii) displays a time-series of a horizontal line normal to the direction of motion of the source.

For $S \ll 1$ (figure 10*a*), particles remain coupled to the initial plume as it descends and the dynamics are comparable to those of single-phase experiments in which $P > P_c$ (§ 3.3). These frames reveal the development of two line vortices in the descending plume, however the features are less distinct than those observed in our single-phase experiments due to the opacity of the particle load. On impact with the base of the tank, the line vorticies spread laterally from the centreline, with the majority of the flow remaining concentrated in the head of the gravity-driven flow. Inspection of the time series presented in figure 10(*a*,iii) shows that after the flow impacts the base of the tank, the high concentration structures spread from the centreline and become separated by a region of low particle concentration. As the flow spreads laterally, sedimentation begins and a sediment deposit forms on the base of the tank.

If the dimensionless separation parameter, S, exceeds unity (figure 10*b*), the fall speed of the particles is greater than the vertical speed of the plume and the particles separate from the flow prior to impacting the base of the tank. In this case, the particles settle from the plume (dark region below the plume in figure 10(*b*,i)) and settle through the ambient at a speed close to their Stokes fall speed whilst being advected by the relative motion of the surrounding fluid (James *et al.* 2022) to form a sediment deposit on the base of the tank. After the particles have separated from the flow, the neutrally buoyant plume fluid

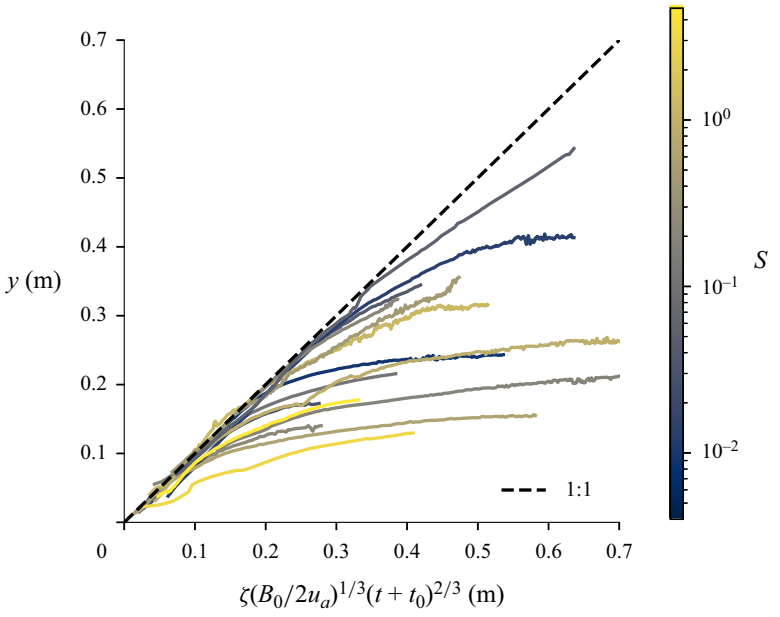

Figure 11. Position of the outer edge of the gravity current with the relation for a 2-D finite release single-phase gravity current (3.9). Each line is coloured according to the dimensionless separation parameter, S, in the experiment.

continues to descend to the base of the tank. The generation of vorticity in the flow prior to the separation of particles leads to the formation of two localised line structures that spread out on impact with the tank flow and then quickly come to rest (figure 11*b*,iii).

4.2. *Quantitative observations*

While the dimensionless parameter $S \ll 1$, the particles remain coupled to the plume and impact the base of the tank to form a particle-driven gravity current. We expect that the initial lateral propagation of the flow to be analogous to that of a 2-D finite release gravity current and follow the relation expressed in (3.9). In figure 11, we compare the position of the outer edge of the gravity-driven flow with (3.9). In this figure, the colours of each line corresponds to a different value of S as shown in the legend. As with our analysis in § 3.3, we assume there is a virtual origin to account for the initial volume of the gravity current imposed by the volume of the plume on impact, and we determine the value of ζ using the method described in § 3.3 and find ζ in the range $\zeta = 1.1$–1.4, consistent with the value of ζ obtained from our single-phase experiments. This data illustrates that for experiments in which $S \ll 1$ (dark blue lines) the initial lateral propagation of the gravity current follows (3.9). However, as the flow evolves it reaches a critical distance at which the sedimentation of particles from the gravity current reduces the driving force of the flow and, hence, speed of the flow. As S increases, corresponding to larger fall speeds, the distance at which the propagation of the gravity current begins to diverge from the scaling law associated with a single-phase inertial gravity current decreases. However, on inspection of the sequence of coloured lines in figure 11, the speed of propagation of the particle-driven gravity current in addition to the point at which particle separation leads to a decrease in the speed of current does not solely depend on the dimensionless separation parameter, S.

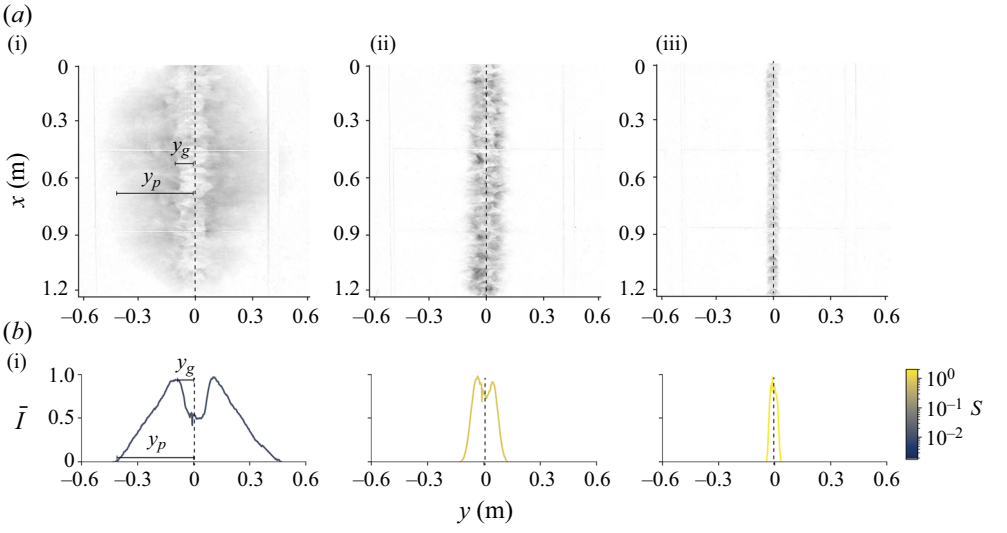

Figure 12. (*a*) Instantaneous images of the base of the tank after an experiment displaying the particle deposits and (*b*) the spatially averaged horizontal light attenuation, $\bar{I}$, profiles of the base of the tank after an experiment. The panels correspond to (i) $S = 0.013$ (experiment 7), (ii) $S = 0.84$ (experiment 9) and (iii) $S = 3.01$ (experiment 10).

To gain further insight into the process of particle sedimentation in these flows, we have analysed the particle deposits that form during an experiment. Figure 12(*a*) displays a series of grey-scale frames of the base of the tank after an experiment, in which we qualitatively illustrate the spatial distribution of the particles. The attenuation of light due to the presence of particles on the base of the tank provides a qualitative indication of the particle concentration of the deposit and is a useful tool to help estimate the distance particles are transported in these flows. To gain an estimate of the time-averaged structure of the particle deposits, we have created a horizontal section of the particle deposit by averaging the normalised light attenuation, $\bar{I}$, profiles along the length of the tank.

Figure 12(*a*,i) and (*b*,i) present the results from an experiment in which $S \ll 1$ and the particles remain coupled to the plume and the mixture impacts the base of the tank to form a particle-driven gravity current. The light attenuation profile reveals that the structure of the deposit consists of a central low concentration region that is bordered by two maximum peaks of equal size that decrease to zero at the edges of the deposit. We define the half width of the central low-concentration region, y_g, as the average distance from the centre of the deposit to the peak light attenuation values, and we define the maximum half-width of the deposit, y_p, as the distance from the centreline of the deposit to the location at which the normalised light attenuation decreases to 5 %. As the particle separation parameter S increases (figure 12*a*,ii and *b*,ii) the maximum width of the deposit decreases and the depth of the central low-concentration region decreases. For $S > 1$ (figure 12*a*,iii–*b*,iii), the maximum width of the particle deposit decreases further and the central low-particle-concentration region is no longer present.

For each of our experiments, we have measured the outer extent of the particle deposit, y_p, and the width of the low-concentration region, y_g, using the light attenuation profiles. In figure 13(*a*), we show the outer extent of the particle deposit, y_p, scaled with the radius of the plume on impact with the base of the tank, $r_p = \beta z_0$. These data reveal that for experiments in which $S > 2$, the maximum extent of the particle deposit is smaller than

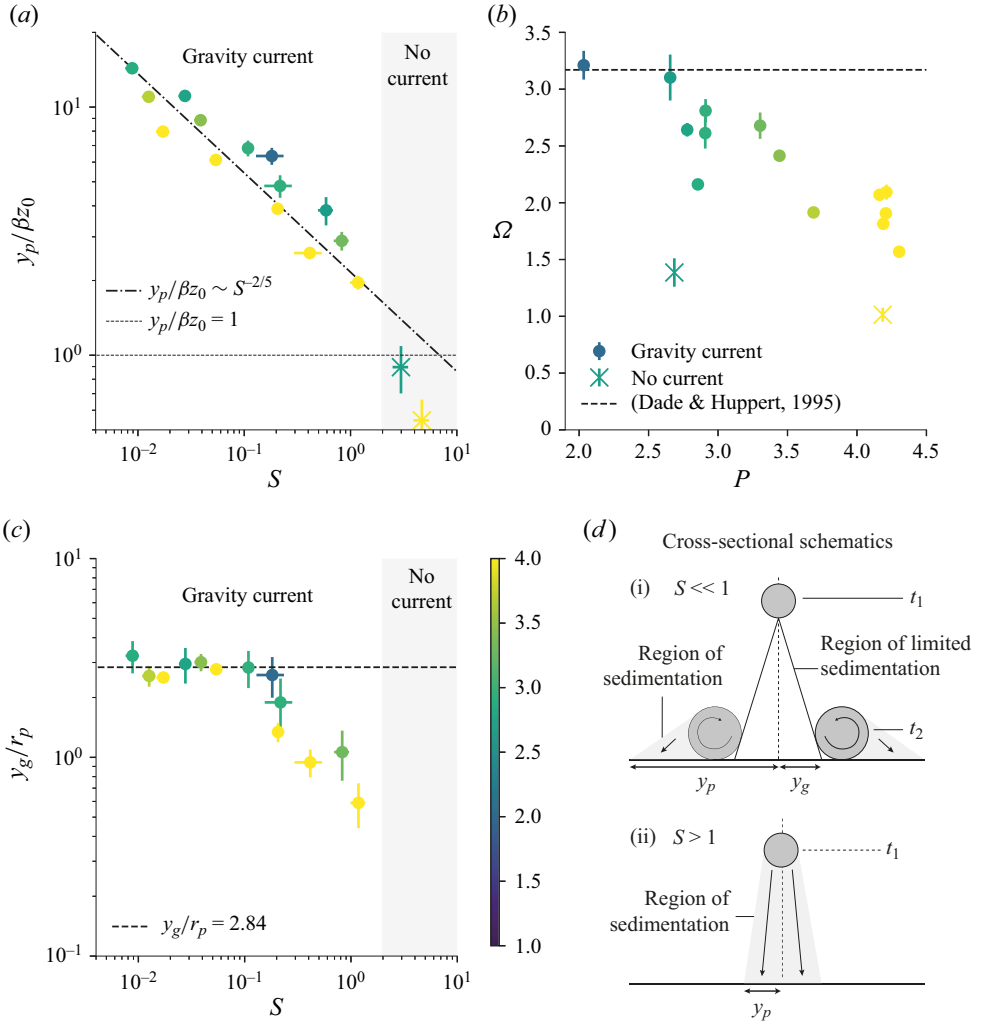

Figure 13. (*a*) The maximum particle dispersal distance, y_p, scaled with radius of the plume on impact, βz_0, with the dimensionless separation parameter, S, on the horizontal axis. The dashed line represents the radius of the of the plume on impact, the dot-dashed line represents the scaling the dispersal distance of particles in a 2-D gravity current (4.1). (*b*) The constant of proportionality, Ω, with the dimensionless source speed, P. The crosses represent experiments in which the particles separate from the plume prior to impacting the base of the tank, the circles represent experiments in which a particle-driven gravity current forms on the base of the tank. The dashed line represents the value of Ω obtained for 2-D finite release gravity currents (Dade & Huppert 1995). (*c*) The half-width of the low-concentration region of the deposits, y_g, scaled with the radius of the plume on impingement, $r_p \sim \beta z_0$, as a function of the dimensionless separation parameter, S. Each point is coloured according to the dimensionless source speed, P. The grey areas represent the region of dimensionless separation parameter, S, in which particles separate from the plume prior to impacting the base of the tank and no gravity current is formed. (*c*) Schematic diagram highlighting the dynamics of particle separation for experiments in which (i) $S \ll 1$ and (ii) $S > 2$.

the radius of the plume on impact with the base of the tank. This suggests that for $S > 2$, the separation of particles occurs in the plume prior to impacting the base of the tank and a particle-driven gravity current is not formed, consistent with our qualitative observations presented in § 4.1.

For our experiments in which the $S < 2$, the particle dispersal distance is much greater than the radius of the plume on impact, and increases as the dimensionless parameter, S, and hence fall speed of the particle load decreases. Here, we appeal to the work of Dade & Huppert (1995) and Harris, Hogg & Huppert (2001) on particle-driven 2-D finite release gravity currents, in which the authors show that the travel distance of a particle-laden gravity current scales according to the relation

$$\frac{y_p}{y_0} = \Omega S^{-2/5}, \tag{4.1}$$

where $y_0 = \beta z_0$ is a characteristic length scale and $\Omega = 3.17$ is a constant of proportionality (Dade & Huppert 1995). We show the scaling (4.1) in figure 13(a) (black dot-dashed line) using a smaller value of Ω, namely $\Omega = 2.6$, and find that our experimental data to leading order follow a similar trend to the line, however we observe a spread in the best fit value of Ω as a function of P, as shown by the colours of each data point according to the legend in figure 13(c). We have calculated the best fit value of Ω for each of our experiments and present the results in figure 13(b). This figure shows that for our experiments in which the dimensionless parameter $P < 2.5$, the value of Ω is consistent with that obtained for 2-D lock-exchange gravity currents (Dade & Huppert 1995). However, as P increases we observe a decrease in the value of Ω, which suggests that as the dimensionless speed of the source increases, the dispersal distance of particles decreases. This observation is consistent with our experimental observations of saline gravity currents when $P > P_c$, in which we find the speed of the gravity current decreases monotonically as P increases (figure 9d). Furthermore, the dependence of the speed of the gravity current and hence the dispersal distance of particles on the dimensionless source speed P, explains the variation observed in the evolution of the outer edge of the particle-driven gravity currents (figure 11) for experiments in which the dimensionless parameter S has similar values.

We have also measured the half-width of the low-particle-concentration region, y_g, that forms in the centre of the particle deposit in our experiments in which $S \ll 1$. Observations from our experiments show that when $P > P_c$, the circulation which develops in the descending plume leads to the localisation of the particles and plume fluid in two line vortex structures which are separated by a region of low concentration. For experiments with small particles ($S \ll 1$) the particle load remains coupled to the plume fluid during the descent of the plume and so particles only separate from the flow after the formation of a gravity current on the base of the tank. This results in a low-particle-concentration region in the deposit on the base of tank, located along the centreline of the plume (figure 13d,i). We expect that the width of this low-concentration region scales with radius of the plume on impact with the base of the tank, $r_p = \beta z_0$. In figure 13(c), we plot the width of the low-concentration region, y_g, scaled by r_p, for each of our experiments and find the length $y_g = 2.84 r_p$ for $S < 0.1$. As the particle separation parameter S increases, the width of the low-concentration region decreases and is not observable for experiments in which $S > 1$, consistent with the observation that in these cases the separation of particles occurs during the descent of the plume (figure 13d,ii).

5. Implications for deep-sea mining

The experiments and analysis presented in this study provide new insight into the dynamics of gravity currents that form as a turbulent plume interacts with a solid surface. These details are of particular importance when considering the dispersal of particles from sediment plumes released as a result of mining in the deep ocean, often termed discharge

plumes. We expect that a typical discharge plume may have an initial particle volume concentration $c_0 \sim 0.01$, with particles of density similar to that of deep-submarine sediments, $\rho_m = 2700\,\mathrm{kg\,m^{-3}}$, and particle diameters in the range, $D_p = 10^{-4}$–10^{-2} m. Given the larger range of particle sizes that occur in the context of deep-sea mining in comparison with those used in this study, we estimate the fall speed of the particles using the method of Ferguson & Church (2004) which tends to Stokes law for small particles and tends to a fall speed with a constant drag coefficient for larger particles, and we assume that the particles are spherical in shape. The discharge rates that supply these flows are expected to be in the range $Q_0 = 0.001$–$1\,\mathrm{m^3\,s^{-1}}$ and, to allow for direct comparison with the present study, we assume that the density of the interstitial fluid is equal to that of the ambient fluid, which in the deep ocean takes an average value, $\rho_a = 1028\,\mathrm{kg\,m^{-3}}$.

With this information we can evaluate the dynamics of such discharge plumes based on the dimensionless parameters introduced in this study. In figure 14, we present two regime diagrams. In figure 14(*a*) we show the height of the plume source above the seafloor, z_0, on the y axis and the source speed or ocean current speed on the x axis for a fixed volume flux, $Q_0 = 10^{-3}\,\mathrm{m^3\,s^{-1}}$. The solid line represents the critical source height at which $P = P_c$ and the dashed line represents the critical source height at which $S = 2$ for a particle size, $D_p = 10^{-5}$ m. In the region labelled *No gravity current downstream*, the descending discharge plume will be bent over ($P > P_c$) and a particle of size, $D_p = 10^{-5}$ m, will tend to separate from the plume prior to impacting the seafloor ($S > 2$), such that no gravity current will form but instead a particle fall deposit. The region labelled *Gravity current downstream* represents the regime in which the descending discharge plume is bent over ($P > P_c$) however a particle of size, $D_p = 10^{-5}$ m, will remain coupled to descending plume and impact the seafloor to form a particle-driven gravity current that evolves downstream from the point of impact and disperses particles a distance, y_p (4.1), from the centreline of the plume. The dotted line represents the conditions at which $S = 0.1$, and below this dotted line the gravity current develops a low-concentration region along the centreline of the flow with a width that scales with the radius of the plume. Finally, in the region labelled *Gravity current upstream* the conditions will result in a plume that impacts the seafloor and spreads in all directions from the point of impact, analogous to the flows studied in § 3.2. We have also plotted the critical source height, z_s, (1.5) above which we expect stratification to play an important role in the dynamics of the flow, as a black solid line, using a typical value of buoyancy frequency for the deep ocean $N \sim 10^{-5}\,\mathrm{s^{-1}}$. Schematic diagrams highlighting the dynamics of the flows in each regime are shown in figure 14(*d*), alongside an idealised schematic, in figure 14(*e*), of a deposit for a flow in which $P > P_c$ and $S > 2$.

In figure 14(*b*) we show height of the source above the seafloor, z_0, on the y axis and the discharge rate of the plume, Q_0, on the x axis, for a fixed current speed $u_a = 0.1\,\mathrm{m\,s^{-1}}$. The solid orange line represents the critical source height at which $P = P_c$, and the dashed orange lines represent the critical source height at which $S = 2$, for a particle with size, $D_p = 10^{-5}$ m. We find that in most cases the operational parameters tend to form discharge plumes in which the plume will be deflected significantly ($P > P_c$) with particles that remain coupled to the plume so that the flow impacts the seafloor to form a particle-driven gravity current ($S < 1$).

In figure 14(*c*), we present the lateral dispersal distances of particles with diameter $D_p = 10^{-4}$ and $D_p = 10^{-5}$ m as function of the source height, z_0. The solid lines represent the estimate for the maximum lateral dispersal distance from the centreline of the flow, $y_p = (\beta z_0)\Omega S^{-2/5}$ (4.1), using the average value of $\Omega = 2.14$ obtained from our experiments. The dashed lines represent the scaling for the width of the low-concentration region along

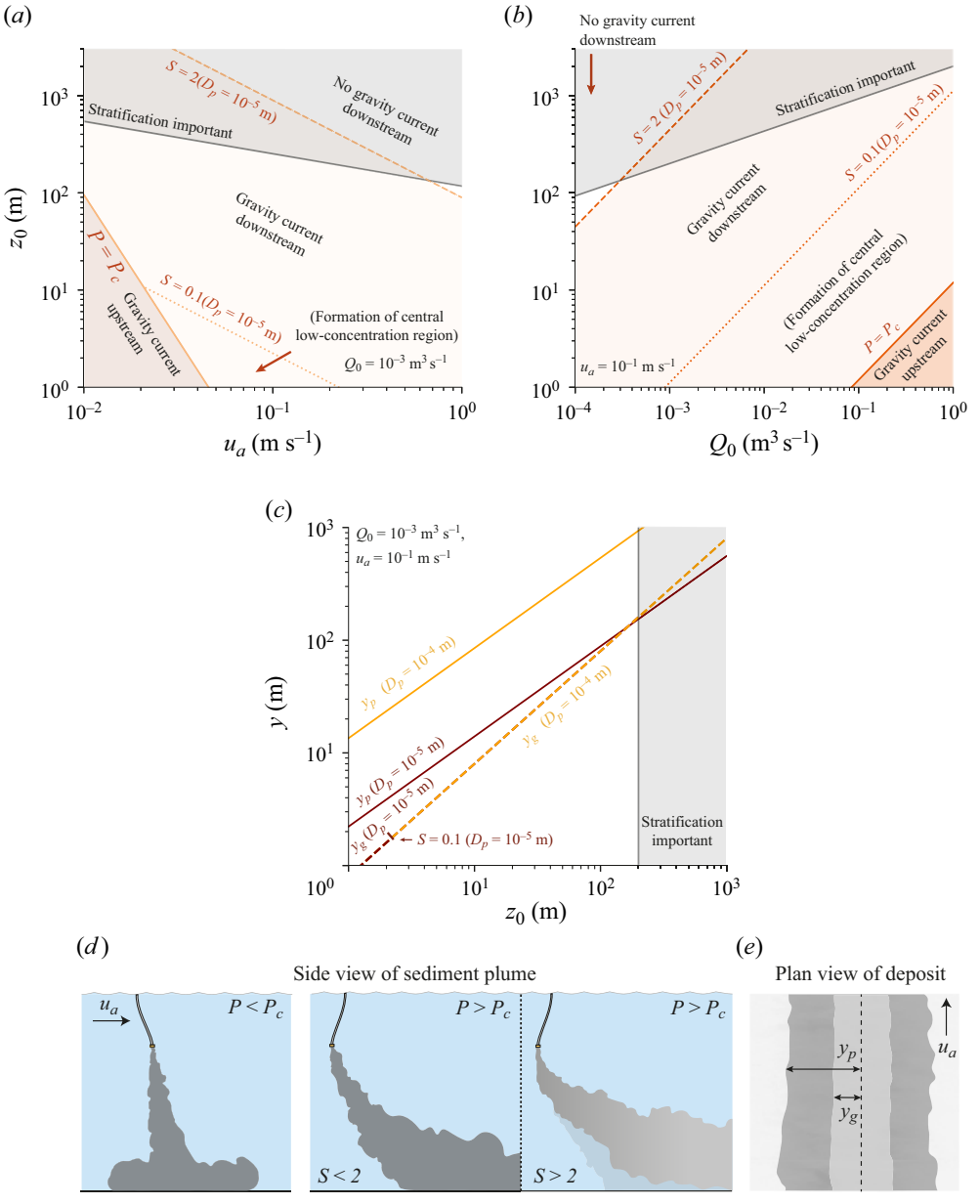

Figure 14. (*a*) The height of the source above the seafloor, z_0, on the vertical axis with the speed of the source/ambient current, u_a, on the horizontal axis for a constant volume flux, $Q_0 = 10^{-3}$ m^3 s^{-1}. The solid line represents the critical source height at which $P = P_c$, and the dashed line represent the critical source height at which $S = 2$, for a particle size, $D_p = 10^{-5}$ m. (*b*) The height of the source above the seafloor, z_0, on the vertical axis and the discharge rate of the plume, Q_0, on the horizontal axis, for a constant current speed $u_a = 0.1$ m s^{-1}. The solid line represents the critical source height at which $P = P_c$, and the dashed line represents the critical source height at which $S = 2$, for a particle size, $D_p = 10^{-5}$ m. (*c*) Lateral dispersal distances of particles with diameter $D_p = 10^{-4}$ and $D_p = 10^{-5}$ m, as function of the source height above the seafloor, z_0. The solid orange and red lines represent the estimates for the maximum lateral dispersal distance from the centreline of the flow, $y_p = (\beta z_0)\Omega S^{-2/5}$ (4.1), using the average value of $\Omega = 2.14$ obtained from our experiments. The dashed orange and red lines represent the scaling for the width of the low-concentration region along the centreline of the flow, $y_g = 2.84 r_p$, for both particle sizes, under the condition $S < 0.1$. (*d*) A series of schematic cartoons illustrating the flow regimes identified in this study and (*e*) a schematic cartoon of the deposit structure when $P > P_c$ and $S \ll 2$.

the centreline of the flow, $y_g = 2.84r_p$, while $S < 0.1$. This graph demonstrates that very small particles may be dispersed distances of order kilometres away from the position of the plume, normal to the motion of the ocean currents, and that a region of low concentration may develop with a width of the order of tens of metres normal to the axis of the plume.

Throughout this study we consider the scenario in which a dense plume issues from a moving source into an ambient environment that is stationary with reference to a solid boundary on which the descending plume impacts and spreads out as a gravity-driven flow. However, in the context of deep-sea mining, dense discharge plumes issue from a moving a vessel into an ocean that is host to currents of varying magnitude and direction. This configuration introduces further complexity to the dynamics of the descending plume and the interaction of the plume with the seafloor, as the direction of the ocean currents may not be in the same direction as motion of the vessel, and the ambient environment may be in motion relative to the seafloor. In addition, the seabed of the deep ocean consists of a highly fluidised mixture of sediment of different sizes. This mobile sediment has the potential to be entrained into a propagating gravity current and, in turn, impact the density evolution and run-out distance of such a flow. Although we do not directly address these complexities in our analysis, we do not expect the leading-order dynamics of these flows and the flow regimes to differ significantly from those presented in this study.

6. Conclusions

In this study we have presented the results of a series of experiments in which we explore the interaction of saline and particle-laden plumes produced from a moving source with a solid surface. We introduce the dimensionless parameter, P, as the ratio of the speed of the source to the characteristic buoyancy speed of the plume, to quantify the effect of the source speed on the morphology and dynamics of the plume and ensuing gravity current. We have determined a value for the critical value, $P_c = 0.83$, which separates the regimes in which after a plume impacts the base of the tank the flow, (i) spreads out in all direction from the point of impact or (ii) propagates exclusively downstream from the point of impact. For $P < P_c$, we have found that the flow propagates radially in a similar fashion to an axisymmetric constant-flux gravity current and tends to a mildly elliptical shape centred about the midpoint of the gravity current, with an aspect ratio that increases as P increases to the critical value. For $P > P_c$, we have observed a transition in the dynamics of the initial plume as the flow becomes bent over and develops circulation in the form of a pair of counter-rotating line vorticies. On impact with the base of the tank, the fluid in the flow remains concentrated in the vortex structures and forms a gravity-driven flow that spreads laterally from the point of impact in a similar fashion to a 2-D finite release gravity current. We have shown that the size of the vortex structures in the gravity currents tend to a constant fraction of the size of the flow, which increases linearly with the dimensionless source speed, P, and that the speed of propagation of the front of the flow decreases as P increases.

We then built on these results to examine the interaction of particle-laden plumes with a solid interface, under the condition that $P > 1$ and introduce the dimensionless separation variable S, as the ratio of the average fall speed of the particle load to the speed of a plume in a crossflow, to quantify the location of particle separation in the flow. We have found that as $S < 2$, particles remain coupled to the fluid in the descending plume and on impact with the base of the tank, the flow transition to particle-driven gravity current. We have observed the formation of a region of low particle concentration in the particle deposit

that reflects the location of fluid in the descending plume as a pair of counter-rotating line vorticies form, with a width that scales with the radius of the plume on impact with the base of the tank. Measurements of the dispersal distance of the particles have revealed that the maximum extent of the particle deposit scales with the scaling for the travel distance of particle-driven 2-D gravity current. We have found that the dispersal distance decreases as the dimensionless source speed, P, increases, consistent with our observations of saline gravity current when $P > P_c$ in which the speed of the gravity current decreases with P. For $S > 1$, we have observed that the particles sediment from the descending plume to form a fall deposit on the base of the tank, with a maximum particle dispersal distance smaller than the radius of the plume on impact. Finally, we have shown the importance of the dimensionless parameters introduced in this study for the analysis of sediment-laden plumes produced as a result of mining in the deep sea.

Funding. This work was supported by the Natural Environment Research Council (grant number 2261860).

Declaration of interests. The authors report no conflict of interest.

Author ORCIDs.
E.L. Newland https://orcid.org/0000-0003-3501-8115.

References

Abdelwahed, M.S.T. 1978 Bifurcation of buoyant jets in cross flow. PhD thesis, McGill University.

Britter, R.E. 1979 The spread of a negatively buoyant plume in a calm environment. *Atmos. Environ.* **13** (1), 1241–1247.

Chen, J.C. & List, E.J. 1976 Spreading of buoyant discharges. In *Proc. Seminar on Turbulent Buoyant Convection*, pp. 171–182. International Centre for Heat and Mass Transfer.

Csanady, G.T. 1965 The buoyant motion within a hot gas plume in a horizontal wind. *J. Fluid Mech.* **22** (2), 225–239.

Dade, W.B. & Huppert, H.E. 1995 A box model for non-entraining, suspension-driven gravity surges on horizontal surfaces. *Sedimentology* **42** (3), 453–470.

Devenish, B.J., Rooney, G.G., Webster, H.N. & Thomson, D.J. 2010 The entrainment rate for buoyant plumes in a crossflow. *Boundary-Layer Meteorol.* **134** (3), 411–439.

Ernst, G.G.J., Davis, J.P., Stephen, R. & Sparks, J. 1994 Bifurcation of volcanic plumes in a crosswind. *Bull. Volcanol.* **56** (1), 159–169.

Ferguson, R.I. & Church, M. 2004 A simple universal equation for grain settling velocity. *J. Sedim Res.* **74** (6), 933–937.

Harris, T.C., Hogg, A.J. & Huppert, H.E. 2001 A mathematical framework for the analysis of particle-driven gravity currents. *Proc. R. Soc.* A **457** (2009), 1241–1272.

Hein, J.R., Koschinsky, A. & Kuhn, T. 2020 Deep-ocean polymetallic nodules as a resource for critical materials. *Nat. Rev. Earth Environ.* **1** (3), 158–169.

Hewett, T.A., Fay, J.A. & Hoult, D.P. 1971 Laboratory experiments of smokestack plumes in a stable atmosphere. *Atmos. Environ.* **5** (6), 767–789.

Hogg, A.J., Hallworth, M.A. & Huppert, H.E. 2005 On gravity currents driven by constant fluxes of saline and particle-laden fluid in the presence of a uniform flow. *J. Fluid Mech.* **539** (1), 349–385.

Hoult, D.P. 1972 Oil spreading on the sea. *Annu. Rev. Fluid Mech.* **4** (1), 341–368.

Hoult, D.P., Fay, J.A. & Forney, L.J. 1969 A theory of plume rise compared with field observations. *J. Air Pollut. Control Assoc.* **19** (8), 585–590.

Hoult, D.P. & Weil, J.C. 1972 Turbulent plume in a laminar cross flow. *Atmos. Environ.* **6** (1), 513–531.

Huppert, H.E. & Simpson, J.E. 1980 The slumping of gravity currents. *J. Fluid Mech.* **99** (4), 785–799.

James, C.B.G., Mingotti, N. & Woods, A.W. 2022 On particle separation from turbulent particle plumes in a cross-flow. *J. Fluid Mech.* **932** (A45), 1–15.

Jones, B., Elliott, R.J.R. & Nguyen-Tien, V. 2020 The EV revolution: the road ahead for critical raw materials demand. *Appl. Energy* **280** (115072), 1–23.

Jones, D.O.B., *et al.* 2021 Environment, ecology, and potential effectiveness of an area protected from deep-sea mining (Clarion Clipperton Zone, Abyssal Pacific). *Prog. Oceanogr.* **197**, 102653.

Kaye, N.B. & Hunt, G.R. 2007 Overturning in a filling box. *J. Fluid Mech.* **576** (1), 297–323.

MARINO, B.M., THOMAS, L.P. & LINDEN, P.F. 2005 The front condition for gravity currents. *J. Fluid Mech.* **536** (1), 49–78.

MINGOTTI, N. & WOODS, A.W. 2015 On the transport of heavy particles through an upward displacement-ventilated space. *J. Fluid Mech.* **772**, 478–507.

MINGOTTI, N. & WOODS, A.W. 2022 Dynamics of sediment-laden plumes in the ocean. *Flow* **2** (E26), 1–26.

MUÑOZ-ROYO, C., *et al.* 2021 Extent of impact of deep-sea nodule mining midwater plumes is influenced by sediment loading, turbulence and thresholds. *Commun. Earth Environ.* **2** (148), 1–16.

NEWLAND, E.L. & WOODS, A.W. 2021 On particle fountains in a stratified environment. *J. Fluid Mech.* **917** (A22), 1–22.

OTSU, N. 1979 A threshold selection method from gray-level histograms. *IEEE Trans Syst. Man Cybern.* **9** (1), 62–66.

OUILLON, R., KAKOUTAS, C., MEIBURG, E. & PEACOCK, T. 2021 Gravity currents from moving sources. *J. Fluid Mech.* **924** (A43), 1–25.

OUILLON, R., MUÑOZ-ROYO, C., ALFORD, M.H. & PEACOCK, T. 2022 Advection-diffusion settling of deep-sea mining sediment plumes. Part 2. Collector plumes. *Flow* **2** (E23), 1–18.

PATTERSON, M.D., SIMPSON, J.E., DALZIEL, S.B. & VAN HEIJST, G.F. 2006 Vortical motion in the head of an axisymmetric gravity current. *Phys. Fluids* **18** (4), 1–8.

SAMASIRI, P. & WOODS, A.W. 2015 Mixing in axisymmetric gravity currents. *J. Fluid Mech.* **782** (R1), 1–13.

SCORER, R.S. 1958 *Natural Aerodynamics*, International Series of Monographs on Aeronautical Sciences and Space Flight, vol. 1, pp. 186–217. Pergamon.

SHARMA, R. 2017 *Deep-Sea Mining: Resource Potential, Technical and Environmental Considerations*, 1st edn. Springer International Publishing.

SHER, D. & WOODS, A.W. 2015 Gravity currents: entrainment, stratification and self-similarity. *J. Fluid Mech.* **784** (1), 130–162.

SHER, D. & WOODS, A.W. 2017 Mixing in continuous gravity currents. *J. Fluid Mech.* **818** (R4), 1–15.

SLAWSON, P.R. & CSANADY, G.T. 1967 On the mean path of buoyant, bent-over chimney plumes. *J. Fluid Mech.* **28** (2), 311–322.

TURNER, J.S. 1960 A comparison between buoyant vortex rings and vortex pairs. *J. Fluid Mech.* **7** (3), 419–432.

TURNER, J.S. 1966 Jets and plumes with negative or reversing buoyancy. *J. Fluid Mech.* **26** (4), 779–792.

UNGARISH, M. 2022 On simple models for gravity currents from moving sources. *J. Fluid Mech.* **952** (A24), 1–19.

ZHANG, X. & GHONIEM, A.F. 1993 A computational model for the rise and dispersion of wind-blown, buoyancy-driven plumes - I. Neutrally stratified atmosphere. *Atmos. Environ.* **27A** (15), 2295–2311.